Self-Organization of CdSe Nanocrystallites into Three-Dimensional Quantum Dot Superlattices

C. B. Murray, C. R. Kagan, M. G. Bawendi*

The self-organization of CdSe nanocrystallites into three-dimensional semiconductor quantum dot superlattices (colloidal crystals) is demonstrated. The size and spacing of the dots within the superlattice are controlled with near atomic precision. This control is a result of synthetic advances that provide CdSe nanocrystallites that are monodisperse within the limit of atomic roughness. The methodology is not limited to semiconductor quantum dots but provides general procedures for the preparation and characterization of ordered structures of nanocrystallites from a variety of materials.

The engineering of materials and devices on the nanometer scale is of considerable current interest in electronics (*1*), optics (*2*), catalysis (*3*), ceramics (*4*), and magnetic storage (*5*). Nanometer-sized crystallites (nanocrystallites) can display optical, electronic, and structural properties that often are not present in either isolated molecules or macroscopic solids. Well-defined ordered solids prepared from tailored nanocrystalline building blocks provide opportunities for optimizing properties of materials and offer possibilities for observing interesting and potentially useful new collective physical phenomena.

Uniform particles, whether atomic, molecular, or colloidal, organize to form ordered solids when attractive and repulsive interparticle forces are properly balanced. Ordered colloids or "colloidal crystals" have attracted scientific attention for more than 50 years and remain an active area of research (*6*). The inherent tendency for monodisperse lyophobic colloids to self-organize provides a general route to new nanostructured materials.

Nanocrystallites of semiconductors have discrete electronic transitions that are tunable with size. They are often referred to as quantum dots (QDs) or artificial atoms. Their highly polarizable excited states are potentially useful in optoelectronic applications (*2*). Collective electronic phenomena have been predicted for three-dimensional (3D) ordered arrays (superlattices) of QDs (*7*). Two-dimensional arrays of substantially larger dots fabricated with the use of lithography show that unusual electronic behavior results from dot interactions (*8*).

In this report we demonstrate that superlattices of nanometer-sized QDs can be generated either in solution as the "crystallization" of a monodisperse colloid or at a solid or liquid interface as a thin, ordered superlattice of dots. In both cases, the size and spacing of the dots are controlled with a precision that is limited by atomic roughness. Assembly at an interface has the added benefit that both the superlattice and the individual dots have their crystallographic axes oriented with respect to the interface, presenting an opportunity to control and study optical anisotropy in the individual crystallites and in the ordered arrays.

Nanocrystallites of CdSe are ideal building blocks for the formation of QD superlattices. Synthetic methods produce macroscopic quantities of single-domain wurtzite crystallites with low defect densities, a uniform shape (slightly prolate along their *c* axis with an aspect ratio of ~1.1 to 1.2), and sizes that are tunable from ~15 to 100 Å in diameter (standard deviation <4%) (*9*). Efficient electronic passivation with a close-packed monolayer of coordinating ligand (trioctylphosphine oxide and selenide) (*10*) gives a room-temperature photoluminescence quantum yield >10%, which is sufficient for the production of electroluminescent devices (*11*). Ligand exchange allows control over the thickness of the organic surface layer and permits derivatization with a broad range of functional groups. Dilute systems of these crystallites have been extensively characterized both structurally (*9*, *10*) and optically (*12*). Close-packed monolayers of these crystallites have been prepared with the use of Langmuir-Blodgett techniques (*13*). A series of small, thiol-capped CdS clusters have also been isolated as single crystals of clusters (*14*).

We are able to prepare QD superlattices with two distinct morphologies: faceted colloidal crystals and ordered thin films. Faceted crystals are produced by homogeneous nucleation in the bulk of the solution. Thin films are formed by heterogeneous nucleation at an interface. In both cases, gentle evaporation with the use of established two-solvent recrystallization methods results in the destabilization of the QD dispersion. Careful regulation of the temperature and pressure allows precise adjustment of the destabilization. QDs capped with trialkylphosphine chalcogenide form a stable dispersion in alkanes but reversibly aggregate in more polar alcohols. A typical procedure involves placing a dispersion of QDs in a mixture of 90% octane and 10% octanol at 80°C under ambient pressure and slowly reducing the pressure. The solution turns opalescent as the lower boiling octane evaporates preferentially over the alcohol, and colloidal crystals form. Initially spreading the solution at an interface maximizes heterogeneous nucleation and produces ordered thin films. Both the colloidal crystals and the ordered thin films require further drying under vacuum to remove all remaining solvents from the superlattice.

Ordered thin films are prepared either at a solid or at a liquid (glycerol) interface. Deposition on solid substrates produces ordered and oriented thin films, whereas evaporation on an immiscible subphase produces free-floating ordered islands. Assembly on Si provides a direct method of integrating these superlattices into existing microelectronic architectures. Optically clear solids of close-packed CdSe QDs are prepared by variation of the deposition conditions to obtain grain sizes that are substantially larger or smaller than the wavelength of light.

Faceted colloidal crystals 5 to 50 μm in size made from CdSe QDs 20 Å in diameter are shown in the optical micrograph of Fig. 1. The crystals were illuminated with polarized white light and photographed with crossed polarization. The yellow color is from depolarized luminescence, the green is from birefringence near the first absorption feature, and the red is from scattering at grain

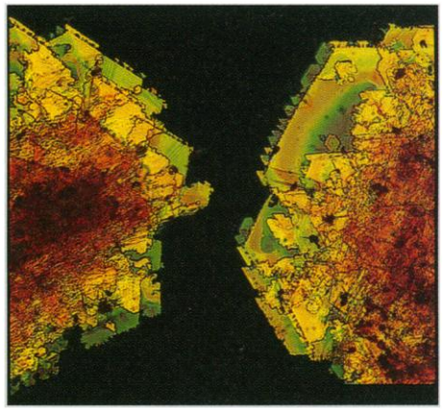

Fig. 1. Dark-field optical micrograph of faceted colloidal crystals. These stacked crystals range from 5 to 50 μm and are formed by self-organization of CdSe QDs 20 Å in diameter. The colloidal crystals are on a quartz slide, back-illuminated with linearly polarized white light and detected at crossed polarization. [Photography by F. Frankel]

C. B. Murray and M. G. Bawendi, Department of Chemistry, Massachusetts Institute of Technology, Cambridge, MA 02139, USA.
C. R. Kagan, Department of Materials Science and Engineering, Massachusetts Institute of Technology, Cambridge, MA 02139, USA.
*To whom correspondence should be addressed.

boundaries in the thicker regions. The faceting and birefringence are macroscopic evidence for both the ordering of the QDs into a 3D array and the net alignment of their unique optical axes within the superlattice.

Optical spectra of close-packed CdSe QDs show the effects of quantum confinement on the individual dots as well as evidence of interdot interactions. Figure 2 (solid lines) shows 10 K optical absorption and photoluminescence spectra of thin solid films of close-packed CdSe QDs that are 38.5 Å (curve a) and 62 Å (curve b) in diameter. The discrete and size-dependent optical absorption features and the band-edge emission are characteristic of the quantized electronic transitions of individual QDs. Comparison of optical spectra for dots close-packed in the solid with dots in a dilute matrix (Fig. 2, dotted lines) reveals that, although the absorption spectra are essentially identical, the emission line shape of the dots in the solid is modified and red-shifted, an indication of interdot coupling.

We investigated the 3D morphology of ordered thin films and of faceted colloidal crystals with high-resolution scanning electron microscopy (HRSEM). Figure 3A shows an HRSEM image of CdSe QDs 64 Å in diameter assembled in rows on an amorphous C substrate and forming terraces and ledges. Each lattice site is occupied by a crystallite containing ~8000 atoms and surrounded by a monolayer of ~600 trioctylphosphine moieties. Figure 3B shows the top of a micrometer-sized colloidal crystal homogeneously nucleated in solution and composed of QDs 48 Å in diameter. Slower growth rates produce larger colloidal crystals with more regular geometries. The characteristic pyramidal shape in Fig. 3C shows the $(100)_{SL}$ faces of a face-centered-cubic (fcc) colloidal crystal oriented along its $\langle 111 \rangle_{SL}$ direction (SL indicates superlattice). The inset of Fig. 3C has the characteristic cubic shape of an fcc crystal oriented along its $\langle 100 \rangle_{SL}$ direction.

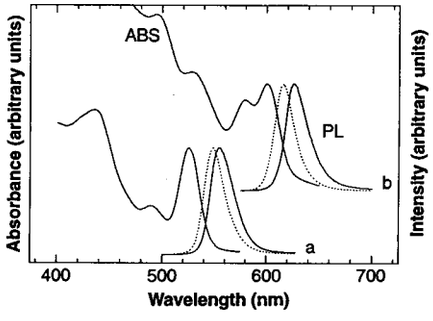

Fig. 2. Optical absorption (ABS) and photoluminescence (PL) spectra at 10 K for close-packed solids (solid lines) of CdSe QDs that are 38.5 Å (curve a) and 62 Å (curve b) in diameter. Dotted lines are photoluminescence spectra of the same dots but in dilute form dispersed in a frozen solution.

Although HRSEM can resolve the positions of individual QDs, more dramatic evidence of ordering is provided by transmission electron microscopy (TEM). Figure 4 shows a portion of a faceted colloidal crystal containing ~500,000 QDs, each 48 Å in diameter. A close-packed monolayer of tributylphosphine oxide on the surface of the dots maintains a 7 Å spacing between the crystallites. Ordered rows of QDs are seen to form sharp edges and vertices.

High-resolution TEM (HRTEM) studies combining real-space imaging and small-angle electron diffraction (ED) can be used simultaneously to probe both the superlattice structure on a micrometer scale and the internal crystal structure of the individual QDs on an angstrom scale. Figure 5A shows an array of CdSe QDs ~64 Å in diameter forming hexagonal close-packed (hcp) sheets. The QDs of one layer are positioned in the interstices of the previous layer. The thickness of this array is ~300 Å (five planes) (*15*). The upper inset shows a close-up of one QD in this superlattice. Internal lattice imaging shows the distinctive columns of Cd and Se atoms representative of the (110) projection of the wurtzite lattice. The ⟨002⟩ or *c* axis of the crystallite (the prolate direction) is lying in the plane of the substrate. The orientation of this crystallite in the superlattice is representative of the majority of the crystallites. The small-angle ED pattern (lower inset) probes an area of the superlattice 2 μm in diameter and characterizes the structure of the superlattice itself. Sharp ED spots demonstrate the lateral perfection of the superlattice on a micrometer scale. We have observed "single-crystal" superlattice ED patterns for domains as large as 100 μm.

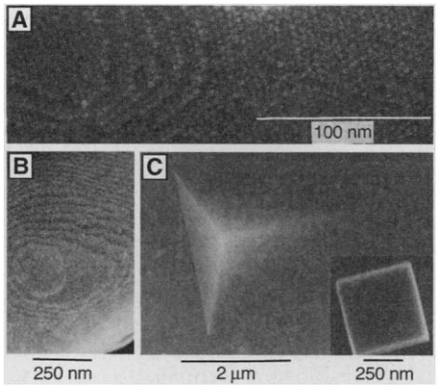

Fig. 3. HRSEM micrographs of 3D QD superlattices. (**A**) Array of CdSe dots 64 Å in diameter on amorphous carbon. Ordered rows of dots form ledges and terraces. (**B**) A micrometer-sized colloidal crystal covered with a light coating of Cr metal shows ledges and terraces closing off to form low-index facets. (**C**) Colloidal crystal of dots 48 Å in diameter showing the characteristic pyramidal shape of a $\langle 111 \rangle_{SL}$-oriented fcc structure. Ledges and terraces have closed to form vicinal $(100)_{SL}$ facets. The inset shows a $\langle 100 \rangle_{SL}$-oriented colloidal crystal from the same sample preparation. Both structures are coated with Au to prevent charging during observation.

Identifying a number of projections of the superlattice allows us to extract a structural model for the 3D array. Although the majority (>80%) of the domains in thin films grow with close-packed $(111)_{SL}$ planes parallel to the substrate, other crystallographic orientations are observed near substrate grain boundaries and defects. Figure 5B shows a $(101)_{SL}$ projection of QDs 48 Å in diameter. This projection is particularly striking because the QDs in each layer are stacked in columns directly on top of each other. The white space around each dot is from the monolayer of organic ligands surrounding each crystallite core. Figure 5C shows the square pattern of a $(100)_{SL}$ fcc projection. The lateral perfection of both projections is displayed in the ED patterns in the insets of Fig. 5, B and C. These TEM surveys support an fcc packing of QDs.

Although electron microscopy provides detailed information on selected areas of a sample, it cannot address statistically large areas. X-ray reflection probes the structure and orientation of both the superlattice (small angles) and the individual crystallites (wide angles) over a large volume of the sample. X-ray reflection is particularly sensitive to the periodicity perpendicular to the substrate. Faceted colloidal crystals grown in solution and an ordered thin film grown on a Si substrate, both from the same initial sample of CdSe crystallites 48 Å in diameter, were studied and compared.

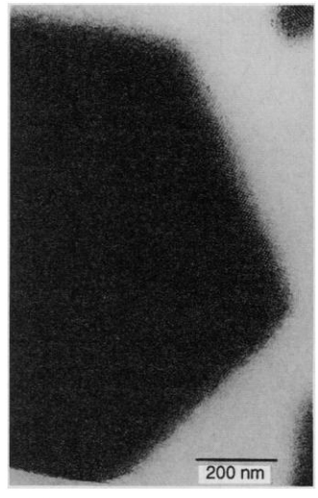

Fig. 4. HRTEM micrograph of a faceted colloidal crystal. Rows of dots 48 Å in diameter capped with tributylphosphine oxide form sharp edges and vertices. The superlattice contains more than half a million QDs.

Curve a in Fig. 6 shows the x-ray diffraction (XRD) pattern of the colloidal crystals. A progression of strong and sharp reflections at small angles covers five orders of magnitude in intensity. The width of the $(111)_{SL}$ reflection is the instrumental resolution. The pattern indicates an fcc packing of dots 48 Å in diameter with an 11 Å spacing of trioctylphosphine moieties between the dots. The intensity of the $(222)_{SL}$ reflection relative to both the $(220)_{SL}$ and the $(311)_{SL}$ is stronger than would be expected if the colloidal crystals were randomly oriented, which indicates a slight preferential orientation of the $\langle 111 \rangle_{SL}$ axes perpendicular to the substrate; this arrangement probably results from the faceted morphology of the colloidal crystals. The positions predicted for the additional reflections of an hcp lattice are marked with asterisks. These contributions may be due to a small number of stacking faults in the superlattice or simply to reflections from particularly thin sections.

Curve b in Fig. 6 shows the XRD pattern for the ordered thin film. The progression of $(hhh)_{SL}$ reflections and the attenuation of the $(220)_{SL}$ and $(311)_{SL}$ peaks at small angles indicate a strong preferential alignment of the $\langle 111 \rangle_{SL}$ axes perpendicular to the substrate, which is consistent with TEM observations.

Thin-film growth allows control over both the orientation of the superlattice and that of the individual QDs. TEM observations indicate that the crystallites tend to align with their elongated *c* axes parallel to the surface. This preferred orientation is unambiguously observed in the wide-angle region of the XRD pattern, which probes the internal structure of the QDs. The wide-angle region for the faceted colloidal crystals (curve a in Fig. 6) shows a pattern consistent with an isotropic distribution of slightly prolate crystallites (9). The wide-angle region of the pattern for the thin film (curve b in Fig. 6) shows a dramatic enhancement of the (110) wurtzite QD reflection, indicating that for >75% of the dots the *c* axis is parallel to the substrate. We have observed >90% alignment in some samples. TEM studies of individual domains show that the QDs are, in addition, aligned with their *c* axes parallel to each other. This arrangement maximizes the van der Waals interactions between neighboring dots and with the substrate.

Control over the size and surface passivation of the individual crystallites results in the precise tailoring of superlattice unit-cell parameters. The left inset in Fig. 6 shows the $(111)_{SL}$ reflections for QD arrays assembled with QDs that have diameters of 63 (c), 54 (d), 47 (e), 39 (f), and 35 (g) Å. The positions of these peaks indicate that the superlattice unit cell increases in size with increasing QD diameter, with the trioctylphosphine capping moieties keeping a constant interdot spacing of 11 ± 1 Å. Collective optical and electrical phenomena due to close packing should result from electronic coupling of the QDs. The strength of this coupling should be tunable by adjustment of the size and electronic properties of the organic layer separating the QDs. We demonstrate control of the spacing between QDs by replacing the trioctylphosphine chalcogenide ligands (8 carbons per chain) with trihexadecylphosphate (16 carbons per chain) and tributylphosphine oxide (4 carbons per chain) surface caps, following the cap exchange method of (9). Curve i in the right inset of Fig. 6 shows the $(111)_{SL}$ reflection for a sample of CdSe crystallites 48 Å in diameter capped with trioctylphosphine oxide groups, indicating a characteristic 11 Å spacing for this capping group. Bulkier hexadecyl groups (curve h) increase the interdot spacing to ~17 Å, and the more compact butyl groups (curve j) produce a 7 Å spacing.

The organic interstices reversibly intercalate a variety of aliphatic and aromatic hydrocarbons. Doping of the superlattice with dye sensitizers, redox-active, or charge-transfer moieties should provide opportunities to functionalize these nanocrystallite arrays. The spacer group can also be removed to provide an entirely inorganic

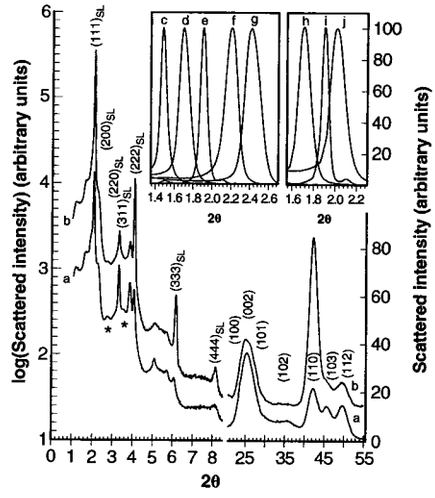

Fig. 6. X-ray diffraction patterns from superlattices. Curve a is the XRD pattern for an ensemble of colloidal crystals of dots 48 Å in diameter. Curve b is the XRD pattern for a $\langle 111 \rangle_{SL}$-oriented thin-film array of dots 48 Å in diameter. The two curves are offset from each other for ease in viewing. The small-angle region is plotted versus the logarithm of the intensity, whereas the large-angle region is plotted versus intensity. Curves c through g are blowups of the $(111)_{SL}$ reflection plotted linearly for arrays assembled with trioctylphosphine oxide–capped dots with diameters of 63 (c), 54 (d), 47 (e), 39 (f), and 35 (g) Å. Curves h through j are blowups of the $(111)_{SL}$ reflection plotted linearly for arrays of 48 Å dots capped with (h) hexadecyl phosphate, (i) trioctylphosphine oxide, and (j) tributyl phosphine oxide, giving interdot spacings of 17, 11, and 7 Å, respectively.

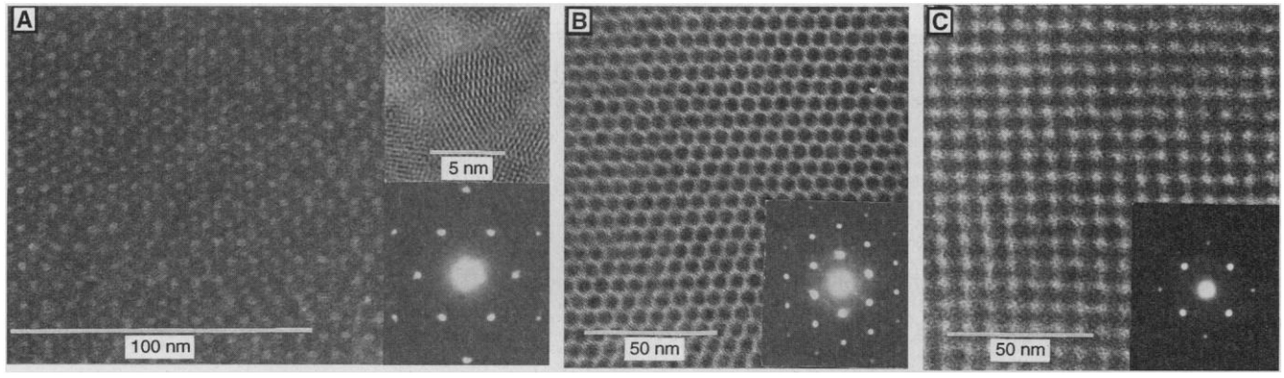

Fig. 5. HRTEM images and ED patterns of QD superlattices for different orientations. (**A**) A $\langle 111 \rangle_{SL}$-oriented array of dots 64 Å in diameter five layers thick. The lower inset shows the small-angle ED pattern; the upper inset is the image of a single 64 Å dot sitting on the top surface of the array with its $\langle 110 \rangle$ axis parallel to the electron beam and its $\langle 002 \rangle$ axis in the plane of the superlattice. (**B**) A $(101)_{SL}$ projection of an fcc array of dots 48 Å in diameter, with the characteristic small-angle ED pattern shown in the inset. (**C**) A $\langle 100 \rangle_{SL}$-oriented fcc array of dots 48 Å in diameter, with the small-angle ED pattern shown in the inset. A Topcon 002B HRTEM was operated at 200 kV for real-space imaging and at 100 kV with a 2-μm aperture for ED experiments.

array. Capping with a volatile species (pyridine) permits the removal of the cap by heating at 150°C under vacuum after formation of the array. QDs in such an array are in intimate contact but are not sintered.

Self-organization is a general phenomenon of colloidal dispersions where control over particle size and stabilization has been achieved. Colloidal crystals are not restricted to simple "monatomic" lattice types. Complex binary superlattices with AB_2 structures (A and B are spheres of different radii) have been found in natural opals (*16*). Examples of AB_2, AB_5, and AB_{13} systems have been prepared with synthetic latex spheres (*16*). Composite colloidal solids have been produced with the use of silica and latex spheres (*17*). Similar complex structures of QDs should be possible.

Colloidal self-organization with nanocrystallites is not restricted to semiconductor QDs (*6*). Self-organization requires only a hard-sphere repulsion, a controlled size distribution, the inherent van der Waals attraction between particles, and a means of gently destabilizing the dispersion. Synthetic routes to monodisperse nanocrystallites of insulating, semiconducting, magnetic, and metallic materials are being pursued by many groups. Manipulation of these diverse materials into superlattices as demonstrated for CdSe QDs in this report should be readily accomplished after control over size distributions and stabilization have been established. The rational design of novel and potentially useful superlattice structures with a variety of nanometer-sized building blocks should then be possible.

REFERENCES AND NOTES

1. M. A. Kastner, *Phys. Today* **46** (no. 1), 24 (1993).
2. L. E. Brus, *Appl. Phys. A* **53**, 465 (1991).
3. L. N. Lewis, *Chem. Rev.* **93**, 2693 (1993).
4. R. Freer, *Nanoceramics* (Institute of Materials, London, 1993).
5. D. D. Awschalom and D. P. DiVincenzo, *Phys. Today* **48** (no. 4), 43 (1995); ———, J. F. Smyth, *Science* **258**, 414 (1992).
6. Opals are a natural example of colloidal crystals; their iridescence is a result of Bragg diffraction of light by 3D arrays of monodisperse, micrometer-sized silica particles [J. V. Sanders, *Acta Crystallogr. Sect. A* **24**, 427 (1967)]. P. Pieranski, *Contemp. Phys.* **25**, 25 (1983) and references therein; P. N. Pusey *et al.*, *Phys. Rev. B* **63**, 25 (1989); S. A. Asher, P. L. Flaugh, G. Washinger, *Spectroscopy* **1** (no. 12), 27 (1986). Colloidal crystallization of nanometer-sized colloids has been demonstrated with 70 Å iron oxide particles [M. D. Bentzon, J. van Wonterghem, S. Morup, A. Tholen, C. J. W. Koch, *Philos. Mag. B* **60**, 169 (1989); M. D. Bentzon and A. Tholen, *Ultramicroscopy* **38**, 105 (1990)].
7. T. Takagahara, *Optoelect. Dev. Tech.* **8**, 545 (1993); *Surf. Sci.* **267**, 310 (1992).
8. D. Heitmann and J. P. Kotthaus, *Phys. Today* **46** (no. 1), 56 (1993).
9. C. B. Murray, D. J. Norris, M. G. Bawendi, *J. Am. Chem. Soc.* **115**, 8706 (1993).
10. L. Becerra, C. B. Murray, R. G. Griffin, M. G. Bawendi, *J. Chem. Phys.* **100**, 3297 (1994).
11. V. Colvin *et al.*, *Nature* **370**, 354 (1994); B. O. Dabbousi *et al.*, *Appl. Phys. Lett.* **66**, 1316 (1995).
12. See, for example, D. J. Norris, A. Sacra, C. B. Murray, M. G. Bawendi, *Phys. Rev. Lett.* **72**, 216 (1994), and references therein.
13. B. O. Dabbousi, C. B. Murray, M. F. Rubner, M. G. Bawendi, *Chem. Mater.* **6**, 216 (1994).
14. G. S. H. Lee *et al.*, *J. Am. Chem. Soc.* **110**, 4863 (1988); N. Herron, J. C. Calabrese, W. E. Farneth, Y. Wang, *Science* **259**, 1426 (1993); T. Vossmeyer *et al.*, *ibid.* **267**, 1476 (1995).
15. We measured this by focusing on the carbon substrate at the edge of the domain and moving radially inward, counting discrete jumps in focal length.
16. J. V. Sanders, *Philos. Mag. A* **42**, 705 (1980); P. Bartlet, R. H. Ottwill, P. N. Pusey, *Phys. Rev. Lett.* **68**, 3801 (1992); M. D. Eldridge, P. A. Madden, D. Frenkel, *Nature* **356**, 35 (1993).
17. J. Th. G. Overbeek, *Adv. Colloid Interface Sci.* **15**, 251 (1982), and references therein.

18. M.G.B. thanks the David and Lucille Packard Foundation and the Sloan Foundation for fellowships. This research was funded in part by NSF grants DMR-91-57491 and ECS-91-18907 and by the NSF-MRSEC program (DMR-94-00034).

26 June 1995; accepted 29 September 1995

Creation of Theta-Auroras: The Isolation of Plasma Sheet Fragments in the Polar Cap

Patrick T. Newell* and Ching-I. Meng

The auroral oval is a ring of luminosity enclosing geomagnetic field lines connected to the solar wind. Occasionally the ring has a bar across it, which seems to imply a bifurcation of the open region. Here results confirm that this "θ-aurora" actually does represent this odd bifurcated configuration, and they demonstrate how it happens. It has hitherto been assumed that θ-auroras occur when the interplanetary magnetic field is directed northward, because that is true of most very-high-latitude arcs. In fact, θ-auroras occur exclusively during the dynamic reconfiguration that follows when the interplanetary magnetic field turns southward after a prolonged northward interval.

When imaged from space in ultraviolet (UV), the Earth wears a halo: A ring of luminosity termed the auroral oval encircles the magnetic poles and has a typical diameter of 36°. Frank, Craven, and co-workers (*1, 2*) have discovered a spectacular effect, namely that the UV image of the polar cap sometimes instead is that of a circle with a bar across it, a phenomenon termed the θ-aurora. The bar (a transpolar arc) runs in the noon-to-midnight direction. It has been suggested that the θ-aurora represents a bifurcation of the Earth's magnetotail plasma sheet, with an isolated splinter of tail plasma being surrounded by geomagnetic field lines that are open to the interplanetary magnetic field (IMF). Aside from the geometry of the images, this suggestion was motivated by ionospheric plasma flow observations indicating antisunward flow surrounding the transpolar arc but sunward flow within it. (Once a magnetic field line becomes connected to the IMF, the general motion of flow must be that of the solar wind, which is antisunward, but field lines in the plasma sheet flow toward the sun.)

However, the same imaging team has cautioned that the isolation of the central arc is not well established (*2*), and doubts about the uniqueness and character of the θ-aurora configuration abound. It is well established that most polar cap arcs occur under IMF $B_z > 0$ conditions (*3, 4*). Theoretically this is because if $B_z > 0$, the

Table 1. The IMF conditions when θ-auroras are first observed.

Date and time (UT)	IMP-8 observations of IMF
	Polar BEAR images
12/16/86 07:17	$B_z < 0$ in sheath after data gap
12/22/86 08:33	$B_z < 0$ after data gap
1/3/87 03:53	No IMF data. Polar cap empty by 04:30 and substorm before 05:40 UT
1/11/87 02:43	$B_z < 0$ after sustained interval > 0
1/15/87 02:57	Data gap, but about 10 min earlier $B_z < 0$ after $B_z > 0$
1/17/87 00:29	$B_z < 0$ after fluctuating about 0
1/27/87 01:58	$B_z > 0$ weakly after variable IMF
2/26/87 01:06	Variable B_z in sheath after $B_z > 0$
3/2/87 03:07	IMP-8 and DMSP F7 data gap
	DE-1 cases reported in literature
10/17/81 17:00	No IMF
10/31/81 22:45	$B_z < 0$ after interval of $B_z > 0$
11/8/81 15:45	No IMF
11/25/81 11:30	No IMF
8/3/86 17:45	$B_z < 0$ after interval of $B_z > 0$